FISEVIER

Contents lists available at ScienceDirect

# Journal of Membrane Science

journal homepage: www.elsevier.com/locate/memsci





# Preparation of defect-free asymmetric gas separation membranes with dihydrolevoglucosenone (Cyrene<sup>TM</sup>) as a greener polar aprotic solvent

Alexander T. Bridge, Benjamin J. Pedretti, Joan F. Brennecke, Benny D. Freeman \*

John J. McKetta Jr. Department of Chemical Engineering, The University of Texas at Austin, 200 E. Dean Keeton Street, Austin, TX, 78712, USA

#### ARTICLE INFO

Keywords:
Dihydrolevoglucosenone (Cyrene<sup>TM</sup>)
Nonsolvent-induced phase separation
Defect-free
Polysulfone
Gas separation

#### ABSTRACT

Nonsolvent-induced phase separation (NIPS) is widely used to prepare asymmetric gas separation membranes. Most industrial NIPS casting solution formulations are limited to a small group of glassy polymers and, importantly, require toxic polar aprotic solvents such as  $N_iN$ -dimethylacetamide (DMAc),  $N_iN$ -dimethylformamide (DMF), or N-methyl-2-pyrrolidone (NMP). Growing restrictions on the use of such solvents are spurring the search for more benign casting solution formulations that do not compromise membrane performance. This study reports high-flux, defect-free asymmetric polysulfone (PSf) gas separation membranes prepared using dihydrolevoglucosenone (Cyrene  $^{TM}$ ), a polar aprotic solvent that is believed to be safer than DMAc, DMF, and NMP, as the majority casting solution component. Optimized formulations and casting conditions produce membranes with hydrogen permeances exceeding 100 gas permeance units (GPU) and selectivities at or above those of dense PSf films. Dry/wet NIPS membrane performance improved with shorter dry step times and increased Cyrene  $^{TM}$  loadings relative to the volatile solvent, tetrahydrofuran (THF), in the casting solution. The high water-Cyrene  $^{TM}$  Flory-Huggins interaction parameter,  $\chi_{12}$ , and high casting solution viscosities help suppress the formation of skin layer defects and sublayer macrovoids. In some cases, membrane selectivities were influenced by substructure resistance, providing insight into the relationship between sublayer morphology and membrane performance.

#### 1. Introduction

Modern industrial gas separation membranes are often prepared via nonsolvent-induced phase separation (NIPS), first described by Loeb and Sourirajan in 1963 [1]. NIPS converts a homogenous polymeric casting solution, often termed "dope," into a porous membrane upon immersion in a coagulant (i.e., nonsolvent) [2,3]. Water is commonly employed as the coagulant due to its low cost, safety, and strong thermodynamic incompatibility with many membrane polymers, which are often hydrophobic. Solvents considered for NIPS dopes are generally water-miscible [2,3]. NIPS membranes intended for gas separation typically possess an asymmetric structure characterized by a porous sublayer that supports a thin "active", non-porous skin layer responsible for the separation. Because penetrant flux is inversely proportional to membrane thickness, the skin layer is generally very thin, on the order of ~100 nm thick [3].

Asymmetric gas separation membrane production employs a transient "dry" step prior to immersion in nonsolvent (i.e., the "wet" step). During the dry step, simultaneous solvent evaporation and nascent

precipitation of the polymer-rich phase together produce a dense skin top layer and a porous transition layer. The latter can extend up to  $\sim\!10$   $\mu m$  beneath the air-dope interface [4,5]. This transition layer is generally less porous than the remaining sublayer, which forms during the wet step [4–6]. To facilitate skin densification and phase separation during the dry step, dope formulations for gas separation membranes often incorporate high loadings of a secondary volatile solvent and a less volatile, weak nonsolvent (i.e., usually an alcohol) in addition to a primary nonvolatile solvent [4].

Skin layer pinhole defects are commonly observed in membranes prepared via the dry/wet NIPS technique [3,4,7]. These defects allow gases to pass through the active layer via nonselective pore flow mechanisms (i.e., viscous flow or Knudsen diffusion). Various treatments, such as thermal/chemical annealing and caulking with cross-linkable poly(dimethylsiloxane), can mitigate selectivity losses associated with such pinholes [3,8], but these techniques decrease membrane flux and necessitate additional post-processing steps [4,8]. Limited examples of NIPS systems that produce defect-free asymmetric gas separation membranes are available in the open literature, and

E-mail address: freeman@che.utexas.edu (B.D. Freeman).

<sup>\*</sup> Corresponding author.

knowledge concerning defect suppression remains largely qualitative [5].

Every gram of membrane prepared from a typical NIPS dope releases approximately three to six g of solvent upon coagulation. During continuous membrane manufacturing, limiting solvent accumulation in the coagulation bath requires constant water replacement. During flat sheet asymmetric membrane production, wastewater generation can range from 100 to 500 L per  $\rm m^2$  of membrane area, depending on the water replacement rate [9]. A single membrane module generally contains 20–300  $\rm m^2$  of membrane area [3], so the amount of wastewater generated can be substantial. In  $\sim\!\!70\%$  of cases, this wastewater, of which >95% originates from initial membrane coagulation, is sent directly down the drain as-is or with some dilution for treatment at municipal wastewater facilities [9]. Unless a viable solvent-lean alternative is developed, the environmental footprint of membrane manufacturing will remain coupled to the hazards associated with the solvents used in NIPS dopes.

As a solvent-based process that generates contaminated wastewater, membrane manufacturing is at risk of increased regulation worldwide [10,11]. One such example is the European Union's regulation on registration, evaluation, authorization, and restriction of chemicals (REACH) [10,12]. REACH classifies several polar aprotic solvents, including *N,N*-dimethylacetamide (DMAc), *N,N*-dimethylformamide (DMF) and *N*-methyl-2-pyrrolidone (NMP), as substances of very high concern due to their reprotoxicity and includes plans for phasing them out of industrial use [10–12]. These compounds are solvents for many common membrane polymers and are believed to be nearly universal in industrial NIPS dope formulations.

A growing body of literature reports asymmetric membrane fabrication using alternative "green" polar aprotic solvents. Compounds of interest include dimethyl sulfoxide EVOL<sup>TM</sup>, methyl 5-(dimethylamino)-2-methyl-5-oxopentanoate (Rhodiasolv® PolarClean), N-butylpyrrolidinone (NBP), and dihydrolevoglucosenone (Cyrene<sup>TM</sup>) [13]. Room temperature ionic liquids have also been investigated as recyclable alternatives to NMP and DMAc [14]. Cyrene TM is a potential replacement for traditional polar aprotic solvents (i.e., NMP, DMAc, and DMF). It was first reported in 2014 [15] and authorized for sale in the European Union in 2018. Unlike the traditional polar aprotic solvents, which are derived from petrochemicals, Cyrene<sup>TM</sup> is mass-produced from lignocellulosic biomass via the Furacell  $^{\text{TM}}$  process [16]. While comparable as a solvent to NMP and DMAc based on Hansen solubility parameters, Cyrene<sup>TM</sup> lacks the N-alkyl amide group associated with the reprotoxicity of NMP, DMF, and DMAc, has no oral toxicity, low mutagenicity, and low ecotoxicity [17,18]. Additionally, Cyrene<sup>TM</sup> is water-miscible and can dissolve several important membrane polymers including polysulfone (PSf), polyethersulfone (PES), polyetherimide, cellulose acetate (CA), Matrimid<sup>TM</sup> polyimide, and poly(vinylidene fluoride) (PVDF) [17, 19,20].

The commercial availability, performance, safety, and potentially more environmentally friendly nature of Cyrene<sup>TM</sup> relative to DMAc, DMF, and NMP has stimulated increased interest in research on polyvinylpyrrolidone (PVP)/PES, PVDF/PES and CA membranes for water purification [17,19,20]. To our knowledge, no studies have demonstrated the fabrication of *integrally skinned asymmetric membranes suitable for gas separations* (i.e., defect-free) using "green" alternatives to traditional polar aprotic solvents. This study reports the use of Cyrene<sup>TM</sup> as the primary solvent to prepare defect-free, flat sheet asymmetric gas separation membranes from PSf. Dry/wet NIPS casting solution formulations were designed to permit comparison with previous work on preparation of defect-free PSf membranes using DMAc and NMP as the nonvolatile formulation components. Cyrene<sup>TM</sup>-based PSf membranes have performance (i.e., permeance and selectivity) comparable to that of industrial PSf membranes.

#### 2. Materials and methods

#### 2.1. Materials

A low cyclic dimer (LCD) grade of Udel P3500 MB7 polysulfone (PSf)  $(M_n = 19,700 \text{ Da}, M_w = 48,600 \text{ Da}, M_z = 81,200 \text{ Da}, M_w/M_n = 2.46)$  was purchased from Solvay S.A. and used as received. Absolute molecular weight measurements via triple detection gel permeation chromatography were performed by Jordi Labs (Mansfield, MA). Anhydrous inhibitor-free tetrahydrofuran (>99.9%), anhydrous 200 proof ethanol (≥99.5%), anhydrous N.N-dimethylacetamide (99.8%), anhydrous Nmethyl-2-pyrrolidone (99.5%), anhydrous N,N-dimethylformamide (99.8%), and dihydrolevoglucosenone (Cyrene<sup>TM</sup>, ≥98.5%) were purchased from MilliporeSigma and used as received. As-received Cyrene TM was stored over activated 4 Å molecular sieves to limit moisture accumulation. A Millipore Milli-Q Advantage A-10 system fed with RO water produced deionized (DI) water at  $\sim\!23\,^{\circ}\text{C}$  that served as the coagulation medium for membrane fabrication. Methanol (>99.8%) and *n*-hexane (>95%) for solvent exchange were purchased from MilliporeSigma and used as received.

#### 2.2. Casting solution preparation

Dense film casting solutions were prepared by dissolving 2.5% by mass PSf in the solvent. Target quantities of solvent were first added to 20 mL scintillation vials, which were pre-cleaned with dry compressed air. PSf was then weighed separately and added to the solvent. Solutions were stirred at 40–80  $^{\circ}\text{C}$  on a hot plate for at least two days prior to evaporation casting.

To prepare casting solutions for NIPS, target quantities of solvents were mixed in the pre-cleaned 20 mL scintillation vials. Solvents were added in order of increasing room temperature volatility to minimize evaporative losses. The desired quantities of PSf were then weighed separately and added to the solvent mixture. Vials were wrapped in parafilm and stirred at  $40–50\,^{\circ}$ C for at least two days prior to membrane fabrication to prepare visually homogenous casting solutions.

# 2.3. Dense film evaporation casting

Once a homogenous mixture was achieved, any residual dust was removed from the polymer solutions by filtration through a 25 mm polytetrafluoroethylene syringe filter with a nominal pore size of 0.45  $\mu m$ . Filtered solutions were sonicated for at least 30 min to remove dissolved gases and bubbles. Immediately after sonication, the solutions were poured into leveled glass rings inside a vacuum oven, and full vacuum was pulled overnight at room temperature. The next day, the oven temperature was raised to 60 °C for 4 h and then to 100 °C for 1 h. Evaporation casting of PSf/Cyrene  $^{TM}$  solutions required an additional 4-h heating step above PSf's  $T_g$  (i.e., 186 °C) [21] under a constant  $N_2$  flow at atmospheric pressure to remove the Cyrene  $^{TM}$ . Films were removed from the casting rings, soaked in room temperature DI water overnight, and boiled in DI water for 4 h. The resulting films were dried under vacuum at 140–150 °C for 24 h. Solvent removal was verified by thermogravimetric analysis (TGA) as described in more detail in section S10 of the supporting information (SI).

# 2.4. Asymmetric membrane preparation via nonsolvent-induced phase separation (NIPS)

Once a homogenous mixture was achieved, the viscous casting solutions were sonicated for at least 30 min to remove any dissolved gas and bubbles. Solutions were then poured onto a cleaned glass plate, and a 4-inch Gardco doctor blade was used to meter the solution to a uniform thickness of 250  $\mu m$ . The cast solution was left in ambient air at  $\sim\!23~^\circ C$  and 30–55% relative humidity for 5–20 s to undergo the dry step of the membrane formation process. The cast solution was then immersed in a

 $\sim\!23$  °C DI water bath to undergo wet phase separation and complete the membrane formation process. The resulting membranes were left to soak in a beaker filled with DI water for 24 h to leach out residual solvent. Next, solvent exchange was performed by soaking the membranes in methanol for 24 h and n-hexane for 24 h. Solvent-exchanged membranes were dried under vacuum at 140–150 °C for 24 h prior to use. TGA was used to verify solvent removal as described in section S10 of the SI.

#### 2.5. Pure gas permeation

Permeation samples were prepared by first cutting square coupons from the membranes. Dense film thicknesses were measured using digital calipers (Mitutoyo,  $\pm 1~\mu m$  resolution) and ranged from 20 to 30  $\mu m$ . Membrane coupons were epoxied to brass discs with a well-defined center area for mass transfer, and a fiber backing was used to support and protect the downstream face of the films. Permeation samples were imaged using a 600 DPI scanner, and their areas were measured using ImageJ software.

The permeation samples were loaded into a modified high-pressure Millipore filter holder (Cat. No. XX4504700), which served as the permeation cell of a constant-volume variable-pressure vacuum permeator [22]. Following an overnight vacuum degassing step, permeation experiments with  $\rm H_2$ ,  $\rm CH_4$ ,  $\rm N_2$ ,  $\rm O_2$  and  $\rm CO_2$ , in that order, were performed at 35 °C and 2–10 bar upstream pressure, as measured by a Honeywell STJE transducer. The steady state downstream pressure rise was recorded using a MKS Baratron transducer with a 0–10 Torr pressure range. To accommodate the high flux of asymmetric samples, 1–2 L ballast volumes were connected to the downstream volume of permeators. Pressure steps were maintained for at least 6 times the measured time lag to ensure that pseudo steady-state conditions were obtained. Pure gas permeance/permeability values were calculated as described elsewhere [22].

### 2.6. Scanning electron microscopy (SEM) of asymmetric membranes

Membrane cross sections were prepared via cryofracturing in liquid nitrogen (LN2). Membranes were soaked in n-hexane for at least 15 s to fill the pores, then immersed in LN2 for at least 30 s and fractured using flat tweezers. Prior to imaging with a FEI Quanta 650 ESEM (20–30 kV, spot size of 3.0), cross-sections were sputter coated for 90 s at 40 mA using a 40:60 Au/Pt alloy source.

#### 2.7. Viscosity measurements

Viscosity measurements of casting dopes were accomplished using a Discovery HR-2 hybrid rheometer. For lower viscosity solutions (<100 Poise), logarithmic flow sweep experiments were performed with DIN concentric cylinders at shear rates of 0.1–1000 1/s. Higher viscosity solutions (>100 Poise) were characterized using a  $2.0^{\circ}$  cone-and-plate attachment at shear rates of 0.01–100 1/s. Solution viscosities were recorded at the Newtonian plateau. More information on these measurements is available in section S6 of the SI.

### 2.8. Thermogravimetric analysis (TGA)

Solvent removal from dense films and asymmetric membranes prepared from PSf was verified using a TA Instruments Q500 TGA. Sample masses of 5–10 mg were loaded onto a platinum pan, and mass loss was tracked in the temperature range from 25 to 800  $^{\circ}\text{C}$  at a heating rate of 5  $^{\circ}\text{C/min}$ . All experiments were performed using  $N_2$  balance and sample purge flow rates of 10 mL/min.

# 2.9. Determination of Flory-Huggins solvent-polymer ( $\chi_{23}$ ) interaction parameters from static light scattering (SLS) experiments

In this study, the nonsolvent or coagulant is labeled as component 1, the solvent as component 2, and the polymer as component 3. SLS experiments were performed at a fixed angle of  $90^\circ$  with a Brookhaven BI-200SM goniometer equipped with a 20 mW He–Ne laser. For each solvent (2) and polymer (3) pair, 6–7 solutions with concentrations ranging from 0.2 to 1.8 mg/mL were prepared and filtered through a 0.1  $\mu m$  syringe filter. Measured intensities were used to construct Debye plots for calculating the second virial coefficients describing each solvent-polymer system [23]. Flory-Huggins (FH)  $\chi_{23}$  binary interaction parameters were calculated for solvent-polymer mixtures using the corresponding second virial coefficient data [24]. More information on these calculations is available in section S1 of the SI.

# 2.10. Determination of Flory-Huggins nonsolvent-polymer ( $\chi_{13}$ ) interaction parameters from liquid sorption experiments

Sorption experiments were performed by soaking dense polymer (3) samples in liquid nonsolvents (1), a technique adapted from previous work [24]. Prior to soaking, polymer samples were dried overnight under vacuum at 140 °C to remove any sorbed water. After recording the dry polymer mass, triplicates of each polymer-nonsolvent pair were enclosed in 20 mL scintillation vials and monitored until equilibrium sorption was achieved. Polymer sample masses were periodically recorded to determine the average amount of sorbed nonsolvent. Polymer and nonsolvent densities were used to convert sorbed nonsolvent mass fractions into volume fractions. FH  $\chi_{13}$  values were calculated from the equilibrium nonsolvent volume fraction by solving a binary form of the FH equation and assuming a nonsolvent activity of 1 [24]. Sorption data and more information regarding the  $\chi_{13}$  calculation can be found in section S3 of the SI.

# 2.11. Calculation of Flory-Huggins water-solvent ( $\chi_{12}$ ) interaction parameters

Composition-dependent activity coefficients for each water (1)-solvent (2) pair were determined using activity coefficient models. For systems with available vapor-liquid equilibrium data, activity coefficients were calculated using the non-random two liquid (NRTL) model [25], with model parameters obtained from Aspen Plus®. For systems without empirically defined model parameters, the UNIFAC group contribution model was used. Information for both models can be found elsewhere [25,26], and more calculation details are available in sections S4 and S5 of the SI.

### 3. Results and discussion

#### 3.1. Dope formulation

#### 3.1.1. Characterization of binary interactions between dope components

Asymmetric gas separation membrane dope formulations generally require solvent mixtures to prevent skin layer defect formation during NIPS [4,5]. As discussed previously, dry/wet NIPS casting solutions for gas separation membranes often include a relatively nonvolatile solvent, a volatile solvent, and a less volatile nonsolvent (i.e., less volatile than the volatile solvent) [5]. This study explores formulations using Cyrene<sup>TM</sup> as the nonvolatile solvent and THF – one of the only known options that is both water-miscible and a solvent for PSf – as the volatile solvent [4]. Ethanol (EtOH) was chosen as a less volatile nonsolvent for a more direct comparison with previous studies, but several options, including other alcohols and alternative amphiphilic nonsolvents, could be used, provided their vapor pressure did not exceed that of THF [4–6]. Table 1 presents relevant physical property data for the solvents and nonsolvents discussed in this study.

**Table 1**Physical property data for selected solvents and nonsolvents.

Solvent/ Nonsolvent	Molecular Weight (g/mol)	RT Density (g/mL)	T <sub>b</sub> (°C)	T <sub>c</sub> (°C)	Reference
NMP	99.13	1.03	204	449	[27]
DMAc	87.12	0.93	166	384	[27]
DMF	73.10	0.94	153	377	[27]
Cyrene <sup>TM</sup>	128.13	1.25	203	_	[15]
THF	72.11	0.89	66	267	[27]
Ethanol	46.07	0.79	78	242	[27]
Water	18.02	1.00	100	374	[27]

<sup>\*</sup>RT = room temperature;  $T_b$  = normal boiling point;  $T_c$  = critical temperature.

Several authors have stressed the importance of thermodynamic interactions in relation to demixing behavior during NIPS [4,24,28–30]. For a system of nonsolvent/coagulant (1), solvent (2), and polymer (3), the Flory-Huggins (FH) model gives the following expression for the activity of component 1 [31]:

$$\ln(a_1) = \ln(\varphi_1) + (1 - \varphi_1) + \left(\frac{V_1}{V_2}\right)\varphi_2 - \left(\frac{V_1}{V_3}\right)\varphi_3 + (\chi_{12}\varphi_2 + \chi_{13}\varphi_3)(\varphi_2 + \varphi_3) \\
- \chi_{23}\left(\frac{V_1}{V_2}\right)\varphi_2\varphi_3 \tag{1}$$

where

$$\varphi_i = \frac{n_i V_i}{\sum_j n_j V_j} \tag{2}$$

In these equations, R is the gas constant, T is the system temperature, and  $n_i$ ,  $V_i$ , and  $\varphi_i$  are the moles, molar volume, and volume fraction of component i, respectively. The  $\chi_{ij}$  terms represent binary interactions between all possible pairings of system components i and j (i.e., polymer, coagulant, and dope solvents/nonsolvents) [31]. Small  $\chi_{ij}$  values indicate favorable interactions, and vice versa. FH models with concentration-dependent interaction parameters (expressed as  $g_{ij}$  in place of  $\chi_{ij}$ ) can be used to predict the onset of phase separation (i.e., binodal and spinodal curves in a ternary phase diagram) [29,32]. The magnitude of  $\chi_{ij}$  parameters has previously been correlated with dope stability, liquid miscibility, and formation of specific morphological features during NIPS [24,30].

Table 2 presents binary Flory-Huggins  $\chi_{ij}$  parameters describing solvent-PSf and nonsolvent-PSf interactions (i.e.,  $\chi_{23}$  and  $\chi_{13}$ , respectively). Experimental  $\chi_{ij}$  values determined from static light scattering (SLS) ( $\chi_{23}$ ) and liquid sorption ( $\chi_{13}$ ) studies are compared with  $\chi_{ij}$  values predicted using Hansen solubility parameters (HSPs). SI sections S1-S3 present relevant primary experimental data and calculation methods. Cyrene TM-PSf solutions exhibited a refractive index increment close to 0, preventing experimental determination of  $\chi_{23}$  via SLS, so the only  $\chi_{23}$  value available was that estimated via HSPs. All experimental  $\chi_{ij}$  values reported in Table 2 are consistent with literature reference values. Excluding the THF-PSf value, HSP  $\chi_{ij}$  values qualitatively agree with the

**Table 2** Relevant Binary Flory-Huggins solvent(2)-polymer(3) and nonsolvent(1)-polymer(3) interaction parameters ( $\chi_{23}$  and  $\chi_{13}$ ) at 23 °C.

1 2	1 4023	N 13'	
Solvent/Nonsolvent	Experimental $\chi_{ij}$	Hansen $\chi_{ij}$	Literature Reference
DMAc	$0.34 \pm 0.04$	0.37	0.33 [30]
DMF	$\textbf{0.44} \pm \textbf{0.05}$	0.82	0.45 [24]
NMP	$0.22\pm0.02$	0.12	0.24 [33]
Cyrene <sup>TM</sup>	_	0.01	_
THF	$0.46\pm0.08$	0.12	0.39-0.46 [24,33]
EtOH <sup>a</sup>	$1.66\pm0.09$	7.31	1.58 [24]
Water <sup>a</sup>	$4.11\pm0.12$	120	2.5-5.9 [33,34]

<sup>&</sup>lt;sup>a</sup> Indicates a nonsolvent (EtOH) or coagulant (water).

experimentally determined solvent quality order. Our experimental  $\chi_{ij}$  values were in better quantitative agreement with the literature values than with the HSP values.

Based on HSP values, initial reports of Cyrene<sup>TM</sup> compared its solvent properties to NMP and DMAc [15,17], both effective solvents for PSf. The Cyrene<sup>TM</sup>-PSf HSP  $\chi_{23}$  value is lower than that of DMAc-PSf, DMF-PSf, and NMP-PSf, so Cyrene<sup>TM</sup> may be a better nonvolatile solvent for PSf than traditional polar aprotic solvents. By extension, Cyrene<sup>TM</sup>-based dopes should remain stable (i.e., homogenous) at higher loadings of the weak nonsolvent (i.e., EtOH) [35].

Table 3 presents binary water-solvent  $\chi_{12}$  interaction parameters, which provide a quantitative basis for comparing water-solvent miscibility and anticipated demixing rates during NIPS [24], as discussed in more detail in section S8 of the SI. In this table, EtOH, although a weak nonsolvent for PSf, is included to permit an easy comparison of its interaction parameter with those of the other solvents. For consistency with previous studies,  $\chi_{12}$  values are reported at  $\varphi_2 = 0.5$  [4,24]. The  $\chi_{12}$  values determined from Aspen Plus® vapor-liquid equilibrium (VLE) data were calculated using the NRTL activity coefficient model [25], and group contribution  $\chi_{12}$  values were estimated from the UNIFAC activity coefficient model [26]. More information on the calculation methods for these  $\chi_{12}$  values are set forth in section S4 of the SI.

Table 3 shows good agreement between the calculated NRTL  $\chi_{12}$  values and those from the literature. UNIFAC  $\chi_{12}$  estimates lie near or within the range of reported literature values but show some disagreement with NRTL  $\chi_{12}$  values, notably for water-DMAc. Previously, inaccuracies have been noted for UNIFAC activity coefficient estimates for mixtures containing alkylamides [36]. This problem has been addressed via the creation of UNIFAC groups representing the entire NMP, DMF, and DMAc molecules. No water-DMAc group interaction values are available [36–38], so the DMAc group could not be used for UNIFAC calculations in this study. More information on UNIFAC group assignments is provided in section S5 of the SI.

Water-Cyrene<sup>TM</sup> VLE behavior is not reported in the open literature. Unique interactions between these two species may complicate experimental analysis. As shown in Fig. 1, in the presence of water, Cyrene<sup>TM</sup> reversibly reacts to form a geminal diol (CGD), increasing the overall solvent amphiphilicity [40]. After 30 min in aqueous solution at ambient conditions, equilibrium CGD:Cyrene<sup>TM</sup> molar concentration ratios can reach values as high as 6 for low (i.e., ~5 wt%) initial Cyrene<sup>TM</sup> concentrations in water [40]. Because Cyrene<sup>TM</sup>-based asymmetric membranes form within ~30 s during the wet step (see section S8 of the SI), CGD concentrations exceeding that of Cyrene<sup>TM</sup> are not expected during NIPS. Additional information on water-Cyrene<sup>TM</sup> reaction kinetics would help elucidate the effects, if any, of CGD on the demixing behavior of Cyrene<sup>TM</sup>-based NIPS systems.

Based on UNIFAC  $\chi_{12}$  estimates for the water-Cyrene<sup>TM</sup> system, Cyrene<sup>TM</sup> is less water-miscible (i.e., has a higher  $\chi_{12}$  value) than NMP, DMAc, or DMF, so Cyrene<sup>TM</sup> should promote delayed demixing during

**Table 3** Binary coagulant (1)-solvent (2) Flory-Huggins interaction parameters ( $\chi_{12}$ ) for relevant aqueous systems (i.e., water is component 1) at 25 °C. Values are reported at  $\varphi_2=0.5$ .

Solvent	VLE $\chi_{12}$ (NRTL)	Group Contribution $\chi_{12}$ (UNIFAC)	2 Literature Values		
DMAc	0.47	0.13	0.19-0.68 [4,30,38]		
DMF	0.74	0.47	0.60-0.72 [4,30]		
NMP	0.38	0.51	0.18-0.96 [30,33,34, 38]		
Cyrene <sup>TM</sup>	_	0.92	_		
CGD	_	0.33	_		
THF	1.46	1.39	1.40-1.45 [4]		
EtOH <sup>a</sup>	1.02	1.09	1.0 [39]		

<sup>&</sup>lt;sup>a</sup> EtOH is a nonsolvent for PSf and included here to permit facile comparison of its interaction parameter with those of other components.

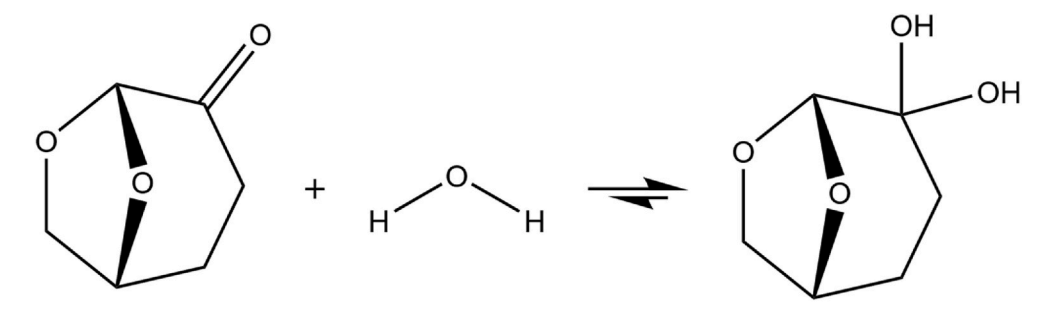


Fig. 1. Reaction of Cyrene<sup>TM</sup> and water to form Cyrene<sup>TM</sup> geminal diol (CGD).

NIPS. The UNIFAC  $\chi_{12}$  prediction for water-CGD indicates that CGD exhibits much higher water affinity than does Cyrene<sup>TM</sup> (i.e.,  $\chi_{12}$  value of 0.33 vs. Cyrene<sup>TM</sup>'s value of 0.92), consistent with the diol group's expected propensity for hydrogen bonding. Thus, the effective  $\chi_{12}$  value describing water-Cyrene<sup>TM</sup> interactions may be somewhat lower than the value estimated for pure Cyrene<sup>TM</sup>. Based on membrane formation experiments with binary solvent-PSf casting solutions, Cyrene<sup>TM</sup>-PSf dopes exhibited greater demixing times (i.e., 20–30 times longer) than those of NMP-PSf, DMAc-PSf, and DMF-PSf dopes. These results are discussed in section S8 of the SI and indicate that CGD formation does not significantly accelerate demixing in PSf-Cyrene<sup>TM</sup> systems.

# 3.1.2. Selection of polymer and nonsolvent concentrations

Previously, Pesek et al. demonstrated the application of dry/wet aqueous NIPS to casting systems based on Udel P1800 PSf. Two solvent blends that used either NMP or DMAc as the nonvolatile solvent were proposed, each incorporating THF as the volatile solvent, with EtOH being used as the less volatile nonsolvent [4]. In this study, "control" dopes were prepared using Pesek's original formulation, which used DMAc as the nonvolatile solvent. This formulation is labeled "M0". For comparison, a new version of the M0 formulation, labeled "M1", was prepared using Cyrene<sup>TM</sup> in place of DMAc.

Although both M0 and M1 contained 22 wt % PSf, Cyrene<sup>TM</sup> is denser than DMAc, and the volumetric PSf concentration was higher in M1, as shown in Table 4. To prepare a sample with the same PSf volume fraction as M0, the PSf mass loading was decreased to 20 wt %, while the solvent ratios were held constant in dope M2. This mass concentration was used for dope formulations M3-M9. As the viscosity data for dopes M0, M1, and M2 in Table 4 show, substitution of DMAc with Cyrene<sup>TM</sup> increases dope viscosity. This result is consistent with Cyrene<sup>TM</sup>'s ability to form highly viscous casting solutions from binary dopes as discussed in section S6 of the SI.

In addition to volatile solvent (i.e., THF) evaporation, which concentrates the polymer in the skin layer, nascent phase separation during the dry step helps accelerate skin layer vitrification prior to bulk phase

separation in the wet step. Phase separation near the skin layer may not be triggered by volatile solvent loss, however, if casting dope nonsolvent loadings are not maximized [5]. Given Cyrene TM's higher PSf solvent strength than that of DMAc as predicted by HSP analysis (i.e., lower  $\chi_{23}$  value, cf. Table 2), Cyrene TM-based dopes were expected to tolerate higher EtOH concentrations than could Pesek et al.'s DMAc-based formulations. Starting with the solvent blend in dope M2, new casting dopes were prepared with EtOH loadings as high as 18 wt %. At the highest EtOH concentrations, homogenous solutions would phase separate shortly after dissolution, despite being sealed in vials. Solutions prepared with 16 wt % EtOH remained stable (i.e., a single, homogenous phase) for several days, so this concentration was selected for dopes M3-M9.

#### 3.2. Membrane morphology

Cross-sectional SEM micrographs of membranes prepared from dopes M0, M1, and M2 are presented in Fig. 2. Each membrane was prepared with a 15-s dry step. Comparing M0 sublayer morphology with that of M1 and M2 membranes, substitution of Cyrene<sup>TM</sup> in place of DMAc visibly limits macrovoid initiation and growth. Thus, Cyrene<sup>TM</sup>-based membranes exhibit more robust and interconnected porous sublayers than those prepared from DMAc. As discussed in more detail in sections S6 and S8 of the SI, the reduced macrovoid size (i.e., macroporosity) in M1 and M2 membranes is consistent with the higher viscosity and, more importantly, lower water miscibility (i.e., higher  $\chi_{12}$  value, which promotes delayed demixing during NIPS) of Cyrene<sup>TM</sup>-based casting solutions relative to those based on DMAc.

Fig. 3 presents the evolution in cross-sectional morphology of membranes prepared from M3-M9 dopes as the Cyrene<sup>TM</sup>:THF solvent volume ratio is increased from 0.43 (i.e., M3) to 2.54 (i.e., M9) at an EtOH mass concentration of 16 wt %. At extreme solvent ratios (i.e., <0.6 or >2.0), membranes M3, M4, M8, and M9 exhibit a finely microporous, macrovoid-free sublayer. Small macrovoids begin to emerge at solvent ratios of 0.71–1.00 (i.e., M5 and M6), consistent with

Summary of all casting dopes (viscosity at 25 °C and composition) prepared and discussed in this study.

Dope ID	Viscosity (P)	PSf Mass Fraction	PSf Volume Fraction	Solvent A	Solvent A Mass Fraction	Solvent B (THF) Mass Fraction	Nonsolvent (EtOH) Mass Fraction	Solvent Volume Ratio (A/B)
MO	$20.1\pm0.4$	0.220	0.168	DMAc	0.318	0.318	0.144	0.946
M1	$56.7\pm1.3$	0.220	0.183	Cyrene <sup>TM</sup>	0.318	0.318	0.144	0.711
M2	$29.4\pm0.6$	0.200	0.165	Cyrene <sup>TM</sup>	0.326	0.326	0.148	0.711
М3	$28.1\pm0.6$	0.200	0.160	Cyrene <sup>TM</sup>	0.240	0.400	0.160	0.427
M4	$30.4\pm0.4$	0.200	0.162	Cyrene <sup>TM</sup>	0.280	0.360	0.160	0.553
M5	$31.6\pm0.7$	0.200	0.165	Cyrene <sup>TM</sup>	0.320	0.320	0.160	0.711
M6	$57.8\pm1.1$	0.200	0.168	Cyrene <sup>TM</sup>	0.374	0.266	0.160	1.000
M7	$101\pm2$	0.200	0.172	Cyrene <sup>TM</sup>	0.450	0.190	0.160	1.684
M8	$131\pm3$	0.200	0.173	Cyrene <sup>TM</sup>	0.475	0.165	0.160	2.047
M9	$163 \pm 4$	0.200	0.175	Cyrene <sup>TM</sup>	0.500	0.140	0.160	2.540

Notes: Solvent B = THF, Nonsolvent = EtOH. Mass fraction errors were generally  $<\pm 0.1\%$  of the measured value. Solvent and nonsolvent densities are reported in Table 1. Conversions from mass fractions to volume fractions are described in section S7 of the SI.

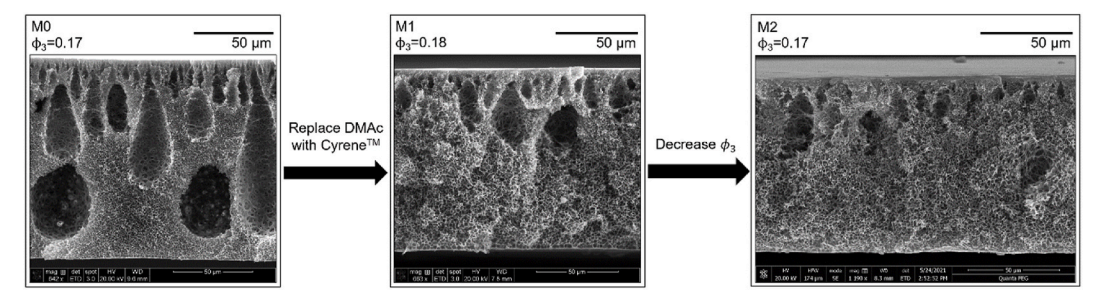


Fig. 2. Cross-sectional SEM micrographs of membranes prepared from M0 (left), M1 (center), and M2 (right).

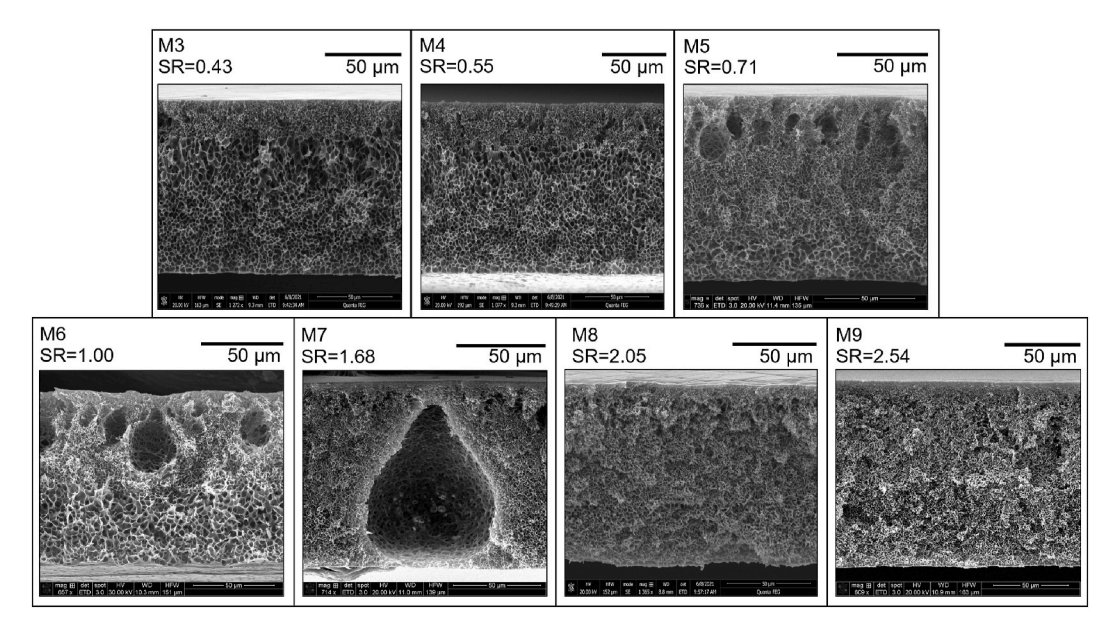


Fig. 3. Cross-sectional SEM micrographs of membranes prepared from dopes M3-M9. Images are ordered by increasing Cyrene  $^{TM}$ : THF solvent volume ratio (SR) used in the dope formulation.

the morphology of M1 and M2 membranes prepared using a solvent ratio of 0.71. M7 membranes were notable outliers, exhibiting sporadic individual macrovoids spanning a large fraction of the sublayer thickness. These macrovoids were generally spaced  $\sim 50-200~\mu m$  apart in the sublayer and were much larger than those present in membranes prepared from dopes M1, M2, M5, and M6. Based on more comprehensive cross-sectional imaging provided in section S9 of the SI, however, the macrovoid content in M7 membranes was still lower than that of M0. Thus, the clear difference in macroporosity between M0 and M3-M9 membranes further confirms Cyrene TM's macrovoid-suppressing

characteristic.

3.3. Comparison of Cyrene  $^{TM}$  and DMAc as nonvolatile solvents for dry/wet NIPS

Table 5 provides relevant pure gas permeation data for selected asymmetric membranes prepared for this study. The gas transport data for all membranes prepared from all dopes is reported in Table S9 in the SI. The permeation properties of dense PSf films prepared from Cyrene<sup>TM</sup> and DMAc as the casting solvents are included for comparison.

Table 5
Selected gas transport data at 35 °C and 2 bar upstream pressure for membranes prepared from dope recipes analyzed in this study. Uncertainty values for membranes M0, M1, M2, and M7 represent 68% confidence intervals calculated from three repeat measurements. Uncertainty values for dense films were calculated via propagation of errors [41].

Casting Dope	Dry Step Evaporation Time (s)	Pure Gas Selectivities (2 bar)				$H_2$ Permeance (GPU – 2 bar)
		H <sub>2</sub> /CH <sub>4</sub>	$H_2/N_2$	$O_2/N_2$	H <sub>2</sub> /CO <sub>2</sub>	
M0 – Pesek et al. <sup>a</sup> [4]	10–15	-	69	6.0	-	221
M0 – This study <sup>b</sup>	15	$77\pm9$	$79 \pm 9$	$6.4 \pm 0.2$	$2.9 \pm 0.2$	$406 \pm 56$
M1 <sup>b</sup>	15	$47 \pm 5$	$53\pm 5$	$\textbf{5.4} \pm \textbf{0.2}$	$2.5\pm0.1$	$62\pm7$
M2 <sup>b</sup>	15	$52\pm 8$	$57\pm7$	$5.7\pm0.2$	$2.4\pm0.2$	$51\pm 6$
M7a <sup>b</sup>	15	$60 \pm 4$	$64 \pm 3$	$5.9 \pm 0.2$	$2.5\pm0.2$	$76\pm2$
M7b <sup>b</sup>	5	$70\pm7$	$72\pm4$	$6.0\pm0.2$	$2.5\pm0.1$	$115\pm10$
PSf – Dense (Cyrene <sup>TM</sup> )	N/A	$59\pm1$	$68\pm1$	$5.9 \pm 0.1$	$2.3\pm0.1$	N/A
PSf – Dense (DMAc)	N/A	$55\pm2$	$\textbf{61} \pm \textbf{2}$	$\textbf{5.9} \pm \textbf{0.2}$	$\textbf{2.1} \pm \textbf{0.1}$	N/A

<sup>&</sup>lt;sup>a</sup> Tested at 24 °C and 50–100 psi (3.4–6.9 bar) upstream pressure.

<sup>&</sup>lt;sup>b</sup> Average properties observed from measurements of three samples.

Cyrene<sup>TM</sup>-cast PSf dense film selectivities were used as performance benchmarks in this work. All gas selectivity values for membranes prepared from M0 were at least as high as those of the dense films, which indicates that the M0 skin layers were defect-free. The defect-free nature of membranes prepared from M0 is consistent with Pesek et al.'s previous study [4]. The higher  $H_2$  gas permeance observed in this study could result from a combination of higher gas permeation temperature (i.e., 35 °C vs. 24 °C used by Pesek et al.) and the difference in PSf grades used for the two studies (i.e., Udel P3500 LCD vs. Udel P1800) [4].

Direct substitution of DMAc with Cyrene  $^{TM}$  in dope M1 reduced the membrane's  $H_2$  permeance relative to that of M0 membranes. Decreasing the polymer concentration in M2 membranes did not significantly impact gas permeance or selectivity beyond experimental uncertainty. In this study, optimum performance was observed with dope M7, which produced membranes with  $H_2$  permeance exceeding 100 GPU and pure gas selectivities comparable to those of M0, on average, when a 5-s dry step was used during casting (i.e., M7b).

In the absence of defects, asymmetric gas separation membranes can exhibit higher gas selectivity than thick (i.e.,  $>10~\mu m$ ) dense films prepared from the same polymer [4]. Because the skin layer thicknesses of these asymmetric membranes are on the order of 100 nm based on  $H_2$  permeance values (cf. Table 5) [4], the physical aging rate is

significantly increased, enhancing the polymer's size sieving behavior and improving selectivity relative to thicker dense films [42,43]. Membranes prepared from M0 and M7b dopes exhibit pure gas selectivities exceeding those of dense PSf.

In this regard, membranes prepared from dopes M1 and M2 exhibited lower selectivity than those of M0 and M7. M1 and M2 still exhibit average  $O_2/N_2$  selectivity values exceeding 90% of the dense film value (i.e.,  $\alpha_D$ ,  $5.9 \pm 0.1$  in this study), an empirical criterion for a defect-free skin [4,6], but their  $H_2/CH_4$  selectivity is, on average, lower (i.e., 73–88% of  $\alpha_D$ ,  $59 \pm 1$  in this study). This behavior is traditionally ascribed to either defective skin layers or substantial substructure gas transport resistance [4,6–8,24]. More detailed plots of permeability and permeance as a function of pressure, as well as gas selectivities, for dense films and asymmetric PSf membranes are provided in sections S11 and S12 of the SI, and these results are also consistent with membranes prepared from dopes M1 and M2 being defect-free.

#### 3.4. Solvent ratio optimization

Previously, the mass ratio of nonvolatile to volatile solvents in casting dopes was found to strongly influence dry/wet NIPS membrane performance [4]. For example, when increasing the DMAc:THF mass

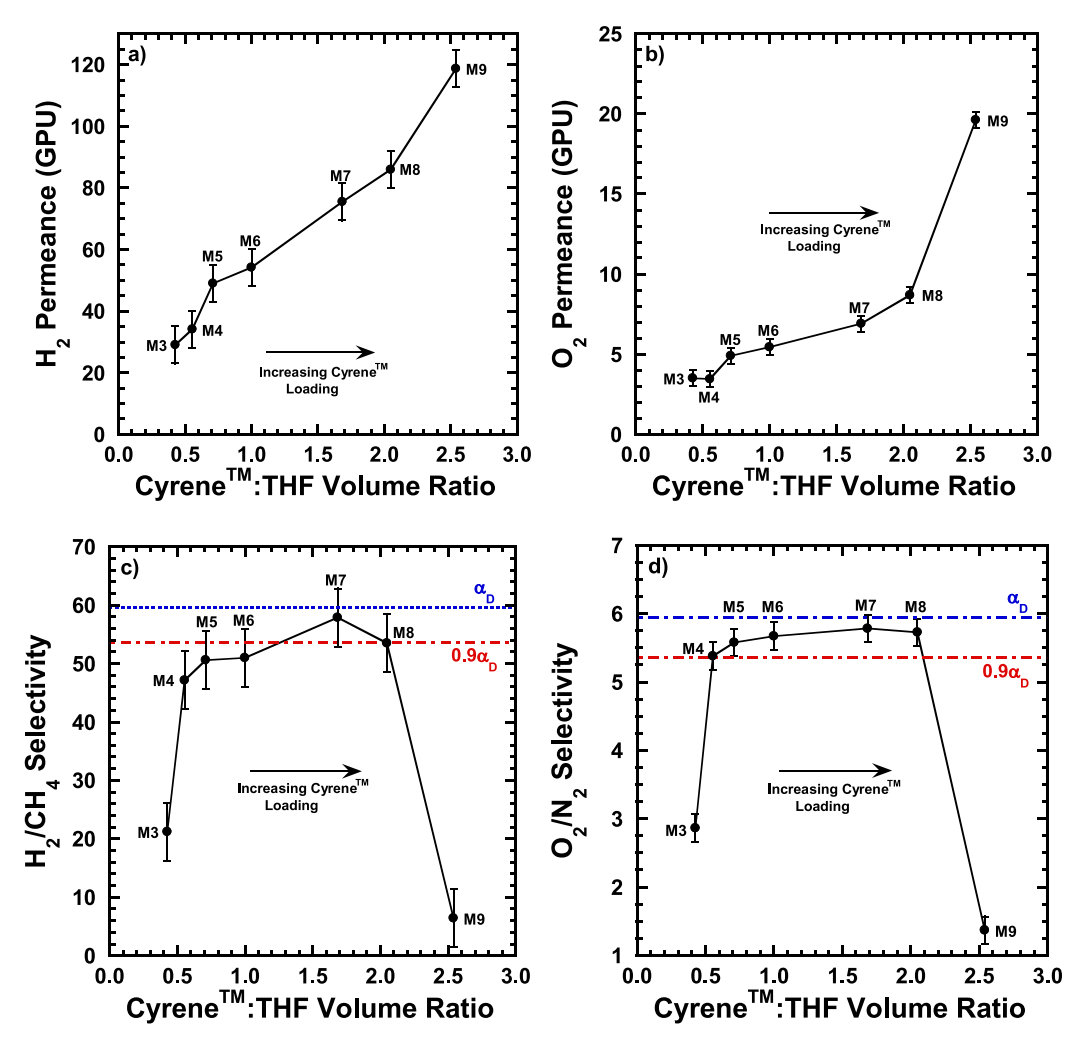


Fig. 4. Influence of solvent volume ratio on gas permeance and gas selectivity for membranes prepared from dopes M3-M9. Performance data is provided for: (a)  $H_2$  permeance (b)  $O_2$  permeance, (c)  $H_2/CH_4$  selectivity, and (d)  $O_2/N_2$  selectivity. All membranes were prepared with a 15-s dry step. Selectivity data is compared to the selectivities of a dense PSf film ( $a_D$ ) prepared from Cyrene<sup>TM</sup>, which are  $59 \pm 1$  and  $5.9 \pm 0.1$  for  $H_2/CH_4$  and  $O_2/N_2$  separations, respectively. Error bars represent the average 68% confidence interval (i.e.,  $\pm 1$  standard deviation) of triplicate repeats of M1, M2, and M7 membranes shown in Table 5. M3 and M9 have defects (see section S12 of the SI). The membrane permeation properties were determined at 35 °C and 2 bar upstream pressure.

ratio in casting solutions, Pesek et al. observed a steady decline in  $O_2/N_2$  selectivity coupled with a rapid increase in  $O_2$  permeance [4]. The positive correlation between membrane permeance and solvent ratio was attributed to decreasing membrane skin layer thickness and a growing population of pinhole defects, which induced selectivity losses.

Several dopes (i.e., M3-M9) were prepared with various volume ratios of Cyrene  $^{TM}$ :THF, all at the same mass loadings of polymer (20 wt %) and nonsolvent (16 wt %), to investigate the effect of solvent ratio on membrane performance. Fig. 4 presents data on the  $\rm H_2/CH_4$  and  $\rm O_2/N_2$  separation performance of membranes prepared from these dopes. Selectivity and permeance data are plotted as a function of the solvent volume ratio, instead of the mass ratio, to account for the density difference between Cyrene  $^{TM}$  and THF.

Based on permeance data in Fig. 4a and b,  $H_2$  and  $O_2$  permeance increases with increasing Cyrene  $^{TM}$ :THF solvent ratio, consistent with the dampened effects of dry step evaporation and phase separation on skin/transition layer formation as the volatile solvent (i.e., THF) fraction is decreased. This relationship is approximately linear for both gases excluding membranes prepared from dope M9. M9 membranes are defective, as evidenced by poor gas selectivity (cf. Fig. 4c and d) and pressure-dependent permeance (cf. Fig. S11) [44]. The loss of selectivity in M9 membranes is presumed to result from insufficient THF evaporation to permit uniform skin layer coalescence (i.e., sealing of pinhole defects) during the dry step [4,5].

Fig. 4c and d exhibit an optimum window for H<sub>2</sub>/CH<sub>4</sub> and O<sub>2</sub>/N<sub>2</sub> selectivity at solvent volume ratios from about 0.5 to 2.0. The maximum selectivity was observed at a solvent ratio of 1.7 (i.e., M7). At the lowest solvent ratio of 0.6 (i.e., M3), skin layer defects again appear, as evidenced by diminished membrane selectivity and pressure-dependent permeance (cf. Fig. S11) [44]. Although high THF loadings should favor skin layer formation, the lower THF solvent strength relative to Cyrene<sup>TM</sup> (i.e., higher  $\chi_{23}$  values, cf. Table 2) decreases dope stability. At a fixed EtOH mass loading of 16 wt %, high THF loadings lead to extensive dry step phase separation, which may introduce a high density of skin layer defects that do not entirely coalesce prior to membrane vitrification [5]. Dopes prepared by Pesek et al. required higher THF loadings (i.e., DMAc:THF ratios of 1-1.5 by mass, 0.9-1.4 by volume) to maintain O2/N2 selectivity values comparable to those of the membranes prepared in this study [4]. This is believed to arise from the lower coagulant-solvent miscibility (i.e., higher  $\chi_{12}$  values, cf. Table 3) of Cyrene<sup>TM</sup>-based casting solutions compared to those based on DMAc, which limits skin layer/sublayer pore formation during NIPS. This concept has been explored in other studies and is discussed further in section S8 of the SI. This phenomenon may influence the differences in selectivity observed in this study.

Fig. 4 selectivity data for membranes cast from dopes M4-M6 and M8 reveals a small discrepancy between H2/CH4 and O2/N2 separation performance, as does data for membranes prepared from dope M1. These membranes all exhibit O2/N2 selectivity values exceeding 90% of the dense film value,  $\alpha_D$ . However, these same samples have  $H_2/CH_4$ selectivities that are somewhat lower than 90% of  $\alpha_D$  in several cases and only equal to 0.9  $\alpha_D$  in the case of M8. The effect is small, within the uncertainty limits for some samples, but it is persistent. As shown in Fig. S11, the relative CH<sub>4</sub> permeance for these membranes decreases with increasing feed pressure, which is expected for dual-mode transport in a defect-free dense PSf film [21]. On this basis, the skin layers of these membranes are defect-free. Curiously, when one qualitatively compares Fig. 4 selectivity data to the sublayer morphology in Fig. 3, selectivity gradually increases with macrovoid emergence and growth in M4-M6, reaches a maximum with the emergence of large macrovoids in M7, and declines as macrovoids disappear in M8. This phenomenon may be related to substructure resistance, which is discussed in more detail below.

#### 3.5. Effect of dry step time on membrane performance

The elapsed time of the dry step is a critical factor in the performance of an asymmetric gas separation membrane [4–6]. As discussed previously, dry step time influences the morphology of two structurally distinct regions: the skin layer and the transition region within the sublayer. Longer dry step times yield higher polymer concentrations at the skin layer, limiting defect formation [5]. As evaporation continues, increased density in the skin and transition layers decreases membrane gas permeance [4]. Optimized dry step times should maximize membrane permeance but still be sufficiently long enough to eliminate skin layer defects.

In the sections above, all membranes were prepared with a dry step time of 15 s. To better understand the contribution of dry step time to Cyrene TM-based PSf membrane performance, formulation M6, which produced membranes with H<sub>2</sub>/CH<sub>4</sub> selectivity values generally lower than 0.9  $\alpha_D$  and O<sub>2</sub>/N<sub>2</sub> selectivity values greater than 0.9  $\alpha_D$ , was compared with M7 (i.e., where both H<sub>2</sub>/CH<sub>4</sub> and O<sub>2</sub>/N<sub>2</sub> selectivities were, on average, greater than 0.9  $\alpha_D$ ) for dry step times ranging from 5 to 20 s. The selectivity and permeance results are presented in Fig. 5.

Membrane permeance data in Fig. 5a and b is consistent with the reported mechanism of membrane formation during the dry step [5,24]. Longer dry step evaporation times generally decreased permeance, consistent with thickness increases in the dense, nonporous skin and/or porous transition layers. Increasing the dry step time did not improve selectivities (cf. Fig. 5c and d). Membranes prepared from dope M6 showed no changes in H2/CH4 or O2/N2 selectivity beyond the limits of experimental error. In contrast, the M7 membrane selectivity decreased as dry step time increased. Maximum selectivities of 70  $\pm$  7 for H<sub>2</sub>/CH<sub>4</sub> and  $6.0 \pm 0.2$  for  $O_2/N_2$  separations were observed for a 5-s dry step time (i.e., M7b). These values agree with the selectivities of membranes prepared from the original DMAc-based Pesek et al. dope, M0, but gas permeance values, while comparable to industrial PSf membranes (i.e., H<sub>2</sub> permeance of 100-200 GPU) [3], are lower than those of M0. For example, the average M0 membrane  $H_2$  permeance was 406  $\pm$  56 GPU (cf. Table 5), and the maximum average H2 permeance of M7 membranes was 115  $\pm$  10 GPU (i.e., M7b, cf. Fig. 5a and Table 5). The lower M7 H<sub>2</sub> permeance could be a consequence of a thicker skin layer and/or lower sublayer porosity relative to M0 membranes. Based on permeance vs. pressure data in Figs. S11b, S12e, and S12f, M7 membranes are defect-free, irrespective of dry step time, so evolving transition layer morphology, rather than skin layer integrity, may be decreasing selectivity as dry step time increases. The rise in  $H_2/CH_4$  selectivity toward  $\alpha_D$ as solvent volume ratio is increased from 1 to 1.7 (i.e., dope M6-M7, cf. Fig. 4), and the difference in response to changing dry step time between membranes prepared from these dopes in Fig. 5, suggest the existence of a critical Cyrene<sup>TM</sup>:THF ratio that, if exceeded, produces a more open transition layer with diminished influence on the selectivities of defect-free membranes prepared in this study.

# 3.6. Theoretical analysis of transition layer contributions to M7 separation performance

The high  $O_2/N_2$  selectivities and pressure-independent permeances indicate that M1, M2, and M4-M8 membrane skin layers are defect-free (cf. Table S9 and Fig. S11). The significantly reduced sublayer macroporosity (i.e., reduced size/density of macrovoids beneath the skin layer) in these membranes relative to those of DMAc-based M0 membranes (cf. Figs. 2 and 3), the qualitative connection between macroporosity and  $H_2/CH_4$  selectivity, and the existence of a critical Cyrene<sup>TM</sup>: THF ratio together suggest that sublayer morphology may contribute to some experimental  $H_2/CH_4$  selectivities being lower than expected (i.e., <0.9  $\alpha_D$ ) based on the  $O_2/N_2$  selectivities being greater than 0.9  $\alpha_D$  for the same membranes. This concept was previously explored by Pinnau et al., who reported that increasing sublayer mass transfer resistance in laminate composites reduced their ability to selectively permeate more

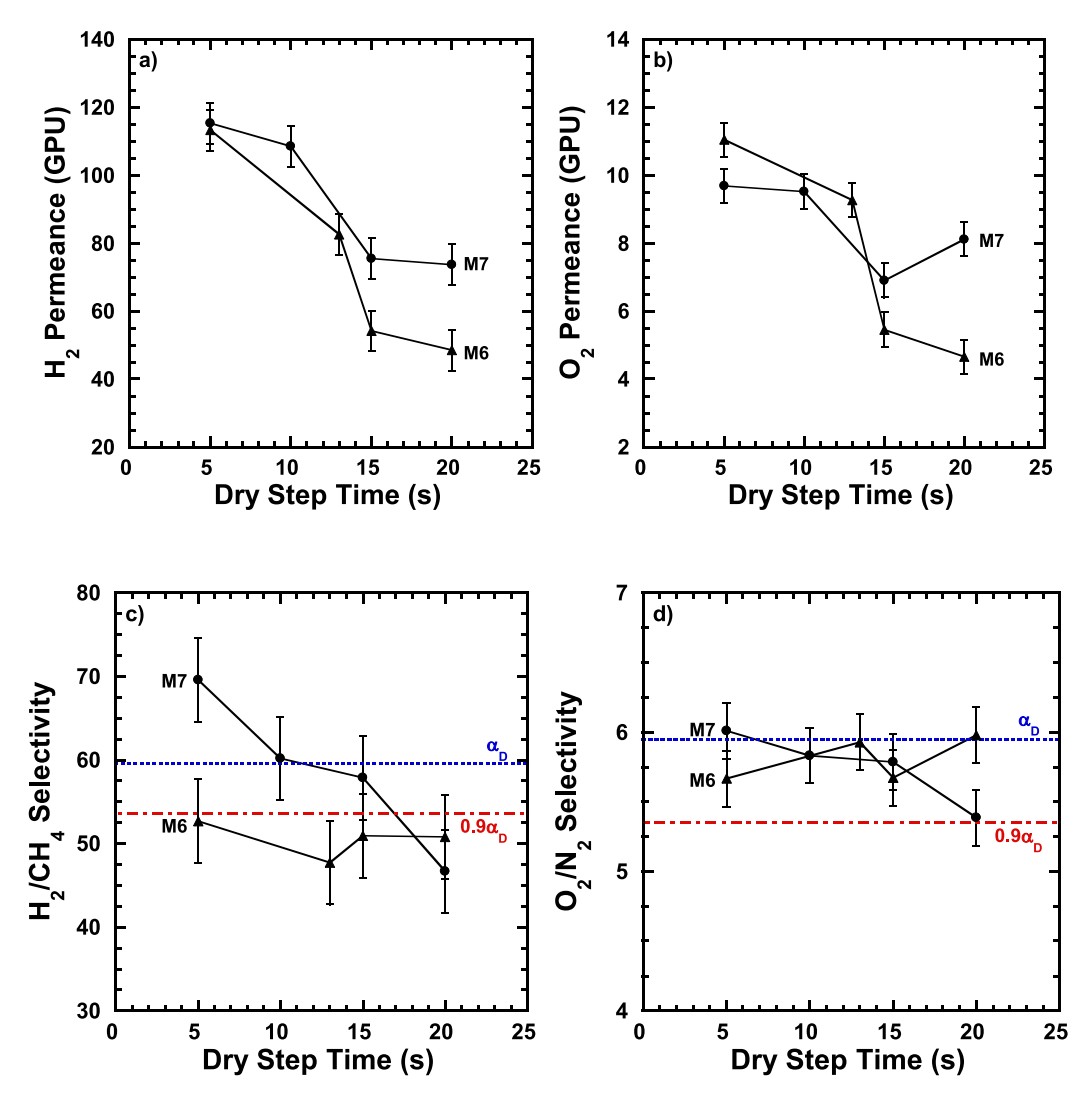


Fig. 5. Influence of dry step time on permeance and selectivity for membranes prepared from dopes M6 and M7. Performance data is provided for: (a)  $H_2$  permeance, (b)  $O_2$  permeance, (c)  $H_2$ /CH<sub>4</sub> selectivity, and (d)  $O_2$ /N<sub>2</sub> selectivity. Selectivity data is compared to the selectivities of a dense PSf film ( $\alpha_D$ ) prepared from Cyrene<sup>TM</sup>, which are  $59 \pm 1$  and  $5.9 \pm 0.1$  for  $H_2$ /CH<sub>4</sub> and  $O_2$ /N<sub>2</sub> separations, respectively. Error bars represent the average 68% confidence interval (i.e.,  $\pm 1$  standard deviation) of triplicate repeats of M1, M2, and M7 membranes shown in Table 5. The membrane permeation properties were determined at 35 °C and 2 bar upstream pressure.

permeable penetrants (i.e.,  $H_2$  and He) [7]. In this study, a similar analysis, presented below, relates increasing sublayer (i.e., transition layer) mass transfer resistance to the decline in defect-free M7 gas selectivities as dry step time is increased from 5 s (i.e., M7b) to 15 s (i.e., M7a).

As discussed in the previous section, the sublayer's transition region, formed principally during the dry step [4,5], may impact overall membrane selectivity in some samples [7]. The Henis and Tripodi resistance model (RM) provides a theoretical basis to investigate the impact of transition layer mass transfer resistance on NIPS membrane transport behavior [8]. This model takes the following form for the permeation of gas a through a membrane consisting of n layers in series:

$$R_{a,T} = R_{a,1} + R_{a,2} + \dots + R_{a,n} \tag{3}$$

$$R_{a,i} = \frac{\ell_i}{P_{a,i}A} = \frac{1}{\varphi_{a,i}A} \tag{4}$$

where  $R_{a,T}$  and  $R_{a,i}$  are the gas a mass transfer resistance for the total membrane and for layer i, respectively.  $\ell_i$ ,  $P_{a,i}$ , and  $\varphi_{a,i}$  are the layer i thickness, gas a permeability, and gas a permeance, and A is the mem-

brane area.

We model the Cyrene TM-based membranes prepared in this study as trilayer structures (i.e., a dense non-porous skin (1), a porous transition layer (2), and a porous support layer (3) which contributes negligible resistance [8]). The transition layer exhibits mass transfer characteristics distinct from those of the dense skin and support layers. Gas permeabilities and selectivities are assigned to the skin layer using experimental data from this study, while mass transfer in the transition layer is presumed to obey Knudsen diffusion [7,24]. Model estimates of total membrane resistance to each gas were evaluated for four different skin layer thicknesses,  $\ell_1$ , with varied transition layer thickness,  $\ell_2$ , and permeability,  $P_{a,2}$ . Skin layer properties (i.e.,  $\ell_1$  and  $P_{a,1}$  values) are representative of M7b membranes (i.e., 5 s dry step), which exhibited minimal evidence of sublayer resistance contributions to membrane performance based on gas selectivities (cf. Table 5), and dense films prepared in this study. The effect of increasing dry step time is manifested in Eqs. (3) and (4) by increasing the thickness or decreasing the permeability of the transition layer, both of which are directly influenced by solvent evaporation and dry phase separation. The model derivation, assumptions, and a more detailed analysis of calculated permeance and selectivity values are presented in section S13 of the SI.

Previously, Pinnau et al. demonstrated that, for any gas a, sublayer resistance contributions to membrane transport and selectivity become significant when the sublayer mass transfer resistance is greater than or equal to about 10% of the mass transfer resistance of the non-porous skin, or, equivalently, when sublayer permeance is less than or equal to 10 times that of the non-porous skin [7]:

$$\frac{R_{a,2}}{R_{a,1}} = \frac{\varphi_{a,1}}{\varphi_{a,2}} \ge 0.1 \tag{5}$$

where  $R_{a,1}$  and  $R_{a,2}$  are the gas a resistance of the skin layer and sublayer, respectively, and  $\varphi_{a,1}$  and  $\varphi_{a,2}$  are the skin layer and sublayer gas a permeance values, respectively.

In Fig. 6, to visualize this case for four hypothesized RM composite membranes, the calculated  $H_2$  and  $O_2$  resistance ratios (i.e.,  $R_{H_2,2}/R_{H_2,1}=\varphi_{H_2,1}/\varphi_{H_2,2}$  and  $R_{O_2,2}/R_{O_2,1}=\varphi_{O_2,1}/\varphi_{O_2,2}$ , respectively) are presented as a function of the thickness of a transition layer (i.e.,  $\ell_2$  values from 1 to 10,000 nm) having a  $H_2$  permeability,  $P_{H_2,2}$ , 50 times ( $\sigma$ ) that of the dense, defect-free skin layer. Knudsen permeability in porous media can vary by several orders of magnitude [3], and this  $\sigma$  value represents one of several considered for this analysis. More information on resistance model calculations involving other  $\sigma$  values is available in section S13 of the SI. For each considered skin layer thickness,  $\ell_1$ , which is fixed in this analysis, the transition layer thickness,  $\ell_2$ , required to match RM composite  $H_2$  permeance to the experimental M7a value, 76 GPU, is marked with a filled black circle. This required  $\ell_2$  value decreases with increasing  $\ell_1$ , and is vanishingly small (i.e.,  $\sim 1$  nm) when  $\ell_1 = 180$  nm.

As demonstrated via the black circles in Fig. 6, the resistance ratio at the  $\ell_2$  value required to match the average experimental M7a H<sub>2</sub> permeance, 76 GPU, exceeds 0.1 for both gases for at least two of the four considered  $\ell_1$  values. This result is consistent with substructure resistance contributions to selectivity losses in M7 membranes as dry step time is increased, in qualitative agreement with the data in Fig. 5a and b. Interestingly, the resistance ratios in Fig. 6 are generally ~3 times higher for H<sub>2</sub> than for O<sub>2</sub>, despite H<sub>2</sub> being the smaller and more permeable penetrant. Thus, predicted H<sub>2</sub>/CH<sub>4</sub> selectivity values diminish more strongly with increasing  $\ell_2$  than those of O<sub>2</sub>/N<sub>2</sub> (cf. Figs. S15c-f). More discussion on the relationship between  $\ell_2$  and RM composite separation performance is provided in Section S13 of the SI. Sublayer resistance contributions may also explain the lower H<sub>2</sub>/CH<sub>4</sub> selectivities (i.e., relative to O<sub>2</sub>/N<sub>2</sub>) of other defect-free membranes prepared in this study (cf. Fig. 4).

Regarding predicted membrane performance, the impact of

decreasing transition layer H<sub>2</sub> and O<sub>2</sub> permeance (i.e., increasing resistance ratio via Eq. (5)) on composite H<sub>2</sub>/CH<sub>4</sub> and O<sub>2</sub>/N<sub>2</sub> selectivity, respectively, is presented in Fig. 7 for  $\sigma = 50$ . All H<sub>2</sub> and O<sub>2</sub> permeance values are calculated from the same range of  $\ell_2$  values considered for Fig. 7 and Fig. S15. Predicted selectivity values diminish more strongly with decreasing transition layer permeance as the skin layer thickness,  $\ell_1$ , is decreased. For example, H<sub>2</sub>/CH<sub>4</sub> and O<sub>2</sub>/N<sub>2</sub> selectivities decline from the dense skin values (i.e., M7b selectivities of 70 and 6.0 for H<sub>2</sub>/ CH<sub>4</sub> and O<sub>2</sub>/N<sub>2</sub> separations, respectively) to the resistance ratio threshold values (i.e.,  $R_{a,2} = 0.1 R_{a,1}$  selectivities of 64 and 5.6 for H<sub>2</sub>/ CH<sub>4</sub> and O<sub>2</sub>/N<sub>2</sub> separations, respectively) at much higher transition layer permeance values (i.e., lower transition layer resistance contributions) when  $\ell_1=100$  nm (i.e.,  $\varphi_{H_2,2}=1370$  GPU and  $\varphi_{O_2,2}=114$ GPU) than for  $\ell_1=180$  nm (i.e.,  $\varphi_{H_2,2}=760$  GPU and  $\varphi_{O_2,2}=64$  GPU). This is consistent with direct proportionality between  $\ell_1$  and  $R_{a,1}$  in Eq. (4). Specifically, decreasing the skin layer's thickness will reduce its resistance contribution to mass transfer of the composite membrane. which enables greater selectivity losses for a given transition layer resistance contribution.

Among the transition layer thickness values that match RM composite H $_2$  permeance (i.e.,  $\varphi_{H_2,T})$  to that of M7a for the four considered skin layer thickness values (indicated in terms of corresponding transition layer permeance for  $\sigma=50$  as filled black circles in Fig. 7), the RM composite membrane with  $\ell_1=160$  nm exhibits similar selectivity properties to that of M7a. More discussion about resistance model approximations relative to M7a properties is provided in section S13 of the SI.

This analysis provides a theoretical basis for  $H_2$  transport being more affected by substructure resistance than other, slower gases, such as  $O_2$ , as dry step time increases. Future studies will include direct characterization of gas transport in the transition/bulk support layers via plasma etching to evaluate resistance model composite predictions and better understand sublayer mass transfer resistance contributions to the performance of Cyrene<sup>TM</sup>-based integrally skinned asymmetric PSf gas separation membranes.

### 4. Conclusions

We report the use of Cyrene<sup>TM</sup>, a potentially safer and less environmentally damaging solvent than those used currently, to prepare defectfree asymmetric gas separation membranes via dry/wet NIPS. The dope solvent volume ratio (i.e., Cyrene<sup>TM</sup>:THF) is an important factor for optimizing membrane performance. Due to the larger water-solvent  $\chi_{12}$ 

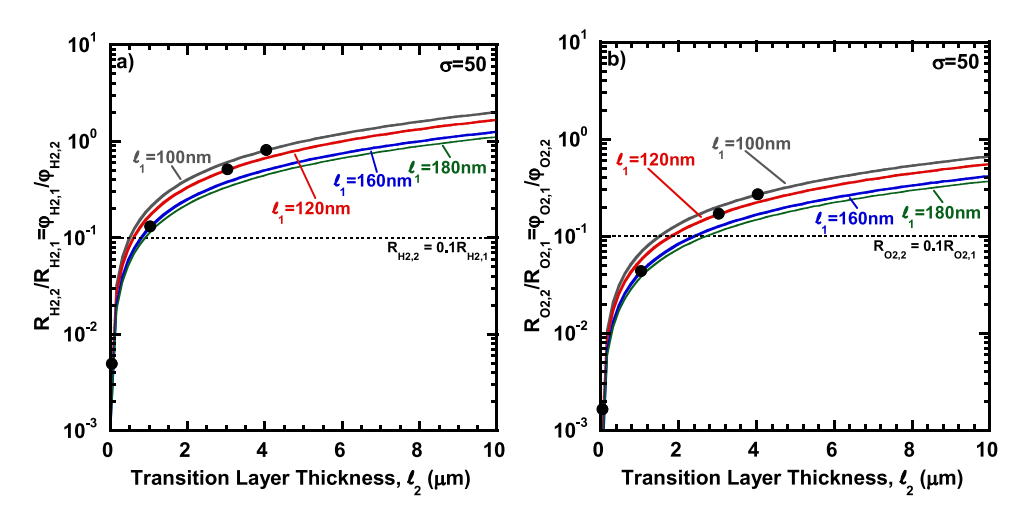
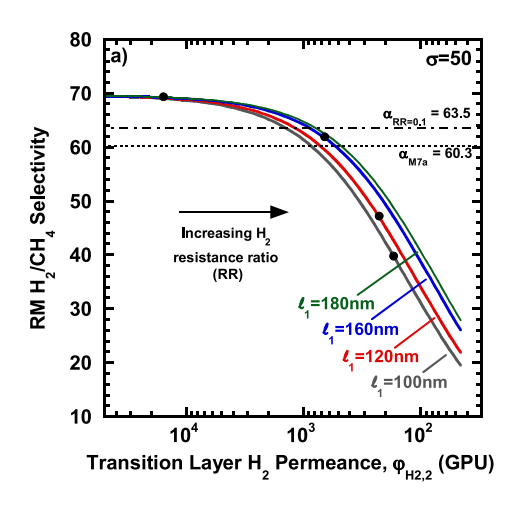


Fig. 6. Resistance model composite (a)  $H_2$  and (b)  $O_2$  mass transfer resistance ratios from Eq. (5) vs. transition layer thickness,  $\ell_2$ , for  $\sigma=50$  and skin layer thicknesses,  $\ell_1$ , of 100, 120, 160, and 180 nm. Transition layer thicknesses that match resistance model predictions to the average experimental M7a  $H_2$  permeance value of 76 GPU are indicated with filled circles.



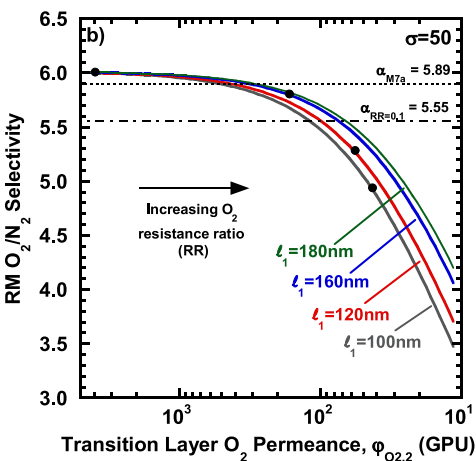


Fig. 7. Resistance model composite membrane (a) H2/CH4 and (b) O2/N2 selectivity vs. transition layer H2 and O2 permeance values, respectively, for  $\sigma = 50$  and skin layer thicknesses,  $\ell_1$ , of 100, 120, 160, and 180 nm. Note that the x-axis is plotted in reverse order (i.e., transition layer permeance values decrease from left to right). Transition layer permeance values calculated from thickness values ( $\ell_2$ ) that match resistance model predictions to the average experimental M7a H2 permeance value of 76 GPU are indicated with filled circles. The resistance ratio (RR) threshold selectivity values for H2/CH4 and O2/N2 separations  $(\alpha_{RR=0.1})$  are indicated with dotted-dashed lines, while M7a H2/CH4 and O2/N2 selectivities ( $\alpha_{M7a}$ ) are indicated with dotted lines. Since skin layer resistance is fixed in this analysis, composite resistance ratio increases with decreasing transition layer permeance and is indicated on both plots.

value in Cyrene TM-based polymer solutions relative to those of traditional, relatively nonvolatile polar aprotic solvents (i.e., DMAc, DMF, and NMP), these casting solutions produce membranes with defect-free skin layers at higher solvent ratios (i.e., lower THF loadings) than previously reported dry/wet NIPS dopes. Cyrene<sup>TM</sup>'s large  $\chi_{12}$  value and ability to produce highly viscous casting solutions also helped minimize sublayer macrovoid formation relative to asymmetric membranes prepared using DMAc as a nonvolatile solvent. Among the defect-free membranes produced, maximum membrane permeance and selectivity values were achieved with formulation M7, which employed Cyrene TM as the majority solvent. M7 membrane preparation with short dry step times (i.e., <10 s) yielded selectivities exceeding those of dense films and increased permeance relative to membranes prepared with longer dry step times. Lower selectivities for dissimilar gas pairs (e.g., H2 and CH<sub>4</sub>) observed for membranes prepared from some dope compositions are hypothesized to result from sublayer resistance rather than skin layer integrity. This theory is supported by resistance model calculations, which demonstrate that transition layer mass transfer resistance increases reduce the flux of faster permeating gases (e.g., H<sub>2</sub>) more than those of larger, slower penetrants (e.g., O2). Future analysis will focus on using direct experimental methods, such as plasma etching, to probe transition layer morphology and permeation properties.

#### **Author statement**

Alexander T. Bridge: Conceptualization, methodology, validation, formal analysis, investigation, data curation, writing – original draft, writing – review & editing, visualization, project administration. Benjamin J. Pedretti: Investigation, writing – original draft, writing – review & editing. Joan F. Brennecke: Writing – review & editing, supervision, project administration, funding acquisition. Benny D. Freeman: Resources, writing – review & editing, supervision, project administration, funding acquisition.

## **Funding sources**

This paper is based upon work supported in part by the National Science Foundation (NSF) under Cooperative Agreement No. EEC-1647722 (A T B., J.F.B., and B.D.F.). Any opinions, findings, and conclusions or recommendations expressed in this material are those of the authors and do not necessarily reflect the views of the NSF. B.J.P.'s work was supported as part of the Center for Materials for Water and Energy Systems (M-WET), an Energy Frontier Research Center funded by the U. S. Department of Energy, Office of Science, Basic Energy Sciences under

Award #DE-SC0019272. The author also thanks the NSF Center for Dynamics and Control of Materials for providing equipment for rheology and light scattering measurements.

#### **Declaration of competing interest**

The authors declare that they have no known competing financial interests or personal relationships that could have appeared to influence the work reported in this paper.

# Acknowledgements

Kevin K. Reimund graciously provided useful discussions about group contribution theory in relation to the estimation of liquid activity coefficients. The authors also thank Ed Sanders and David Hasse for useful discussions about gas transport in porous media.

### Appendix A. Supplementary data

Supplementary data to this article can be found online at https://doi.org/10.1016/j.memsci.2021.120173.

### References

- S. Loeb, S. Sourirajan, Sea water demineralization by means of an osmotic membrane, Saline Water Conversion—II 38 (1963) 117–132.
- [2] G.R. Guillen, Y. Pan, M. Li, E.M.V. Hoek, Preparation and characterization of membranes formed by nonsolvent induced phase separation: a review, Ind. Eng. Chem. Res. 50 (2011) 3798–3817.
- [3] R.W. Baker, Membrane Technology and Applications, third ed., John Wiley & Sons, Chichester, West Sussex; Hoboken, 2012.
- [4] S.C. Pesek, W.J. Koros, Aqueous quenched asymmetric polysulfone membranes prepared by dry/wet phase separation, J. Membr. Sci. 81 (1993) 71–88.
- [5] I. Pinnau, W.J. Koros, A qualitative skin layer formation mechanism for membranes made by dry/wet phase inversion, J. Polym. Sci. B Polym. Phys. 31 (1993) 419–427.
- [6] I. Pinnau, W.J. Koros, Structures and gas separation properties of asymmetric polysulfone membranes made by dry, wet, and dry/wet phase inversion, J. Appl. Polym. Sci. 43 (1991) 1491–1502.
- [7] I. Pinnau, W.J. Koros, Relationship between substructure resistance and gas separation properties of defect-free integrally skinned asymmetric membranes, Ind. Eng. Chem. Res. 30 (1991) 1837–1840.
- [8] J.M.S. Henis, M.K. Tripodi, Composite hollow fiber membranes for gas separation: the resistance model approach, J. Membr. Sci. 8 (1980) 233–246.
- [9] M. Razali, J.F. Kim, M. Attfield, P.M. Budd, E. Drioli, Y.M. Lee, G. Szekely, Sustainable wastewater treatment and recycling in membrane manufacturing, Green Chem. 17 (2015) 5196–5205.
- [10] D. Kim, O.R. Salazar, S.P. Nunes, Membrane manufacture for peptide separation, Green Chem. 18 (2016) 5151–5159.

- [11] H.H. Wang, J.T. Jung, J.F. Kim, S. Kim, E. Drioli, Y.M. Lee, A novel green solvent alternative for polymeric membrane preparation via nonsolvent-induced phase separation (NIPS), J. Membr. Sci. 574 (2019) 44–54.
- [12] L. Bergkamp, N. Herbatschek, Regulating chemical substances under REACH: the choice between authorization and restriction and the case of dipolar aprotic solvents, Review of European, Comp. Int. Environ. Law 23 (2014) 221–245.
- [13] L. Cseri, G. Szekely, Towards cleaner PolarClean: efficient synthesis and extended applications of the polar aprotic solvent methyl 5-(dimethylamino)-2-methyl-5oxopentanoate, Green Chem. 21 (2019) 4178–4188.
- [14] R. Renner, Ionic liquids: an industrial cleanup solution, Environ. Sci. Technol. 35 (2001) 410A–413A.
- [15] J. Sherwood, M. De bruyn, A. Constantinou, L. Moity, C.R. McElroy, T.J. Farmer, T. Duncan, W. Raverty, A.J. Hunt, J.H. Clark, Dihydrolevoglucosenone (Cyrene) as a bio-based alternative for dipolar aprotic solvents, Chem. Commun. 50 (2014) 9650.—9652.
- [16] D.E. Richardson, W.D. Raverty, Predicted environmental effects from liquid emissions in the manufacture of levoglucosenone and Cyrene, Appita J. 69 (2016) 344–351.
- [17] T. Marino, F. Galiano, A. Molino, A. Figoli, New frontiers in sustainable membrane preparation: Cyrene™ as green bioderived solvent, J. Membr. Sci. 580 (2019) 224, 234
- [18] J.E. Camp, S.B. Nyamini, F.J. Scott, Cyrene™ is a green alternative to DMSO as a solvent for antibacterial drug discovery against ESKAPE pathogens, RSC Medicinal Chemistry 11 (2020) 111–117.
- [19] R.A. Milescu, C.R. McElroy, T.J. Farmer, P.M. Williams, M.J. Walters, J.H. Clark, Fabrication of PES/PVP water filtration membranes using Cyrene®, a safer biobased polar aprotic solvent, Adv. Polym. Technol. (2019) 1–15, 2019.
- [20] Y. Wibisono, V. Noviani, A. Ramadhani, A. Baruna, L. Devianto, A. Adi Sulianto, Fabrication of cellulose acetate membrane using cyrene as green solvent, Proceedings 4 (2020) 7189.
- [21] C.L. Aitken, W.J. Koros, D.R. Paul, Gas transport properties of biphenol polysulfones, Macromolecules 25 (1992) 3651–3658.
- [22] H. Czichos, T. Saito, L.R. Smith, Springer Handbook of Materials Measurement Methods, Springer, Germany, 2006.
- [23] Instruction Manual for BI-ZPW Zimm Plot Software for Molecular Weight Determination in Dilute Polymer Solutions, Brookhaven Instruments Corporation.
- [24] I. Pinnau, Skin Formation of Integral-Asymmetric Gas Separation Membranes Made by Dry/wet Phase Inversion, The University of Texas at Austin, 1991.
- [25] R.H. Perry, D.W. Green, J.O. Maloney, Perry's Chemical Engineer's Handbook, seventh ed., McGraw-Hill, New York, 1997.
- [26] A. Fredenslund, R.L. Jones, J.M. Prausnitz, Group-contribution estimation of activity coefficients in nonideal liquid mixtures, AIChE J. 21 (1975) 1086–1099.
- [27] P.J. Linstrom, W.G. Mallard, NIST Chemistry Webbook, NIST standard reference database number 69.

- [28] M.T. So, F.R. Eirich, H. Strathmann, R.W. Baker, Preparation of asymmetric loeb-sourirajan membranes, J. Polym. Sci., Polym. Lett. Ed. 11 (1973) 201–205.
- [29] F.W. Altena, Phase Separation Phenomena in Cellulose Acetate Solutions in Relation to Asymmetric Membrane Formation, University of Twente, 1982, p. 192.
- [30] V.M. Burra, Polymer Phase Inversion Membranes: Effect of Binary Interaction Parameters on Membrane Morphology, Texas Tech University, 1993, p. 117.
- [31] P.J. Flory, Principles of Polymer Chemistry, Cornell University Press, New York, 1953.
- [32] Y.-M. Wei, Z.-L. Xu, X.-T. Yang, H.-L. Liu, Mathematical calculation of binodal curves of a polymer/solvent/nonsolvent system in the phase inversion process, Desalination 192 (2006) 91–104.
- [33] J.Y. Kim, H.K. Lee, K.J. Baik, S.C. Kim, Liquid-liquid phase separation in polysulfone/solvent/water systems, J. Appl. Polym. Sci. 65 (1997) 2643–2653.
- [34] M. Karimi, W. Albrecht, M. Heuchel, M. Kish, J. Frahn, T. Weigel, D. Hofmann, H. Modarress, A. Lendlein, Determination of water/polymer interaction parameter for membrane-forming systems by sorption measurement and a fitting technique, J. Membr. Sci. 265 (2005) 1–12.
- [35] M.A. Frommer, I. Feiner, O. Kedem, R. Bloch, The mechanism for formation of "skinned" membranes II. Equilibrium properties and osmotic flows determining membrane structure, Desalination 7 (1970) 393–402.
- [36] J.C. Bastos, M.E. Soares, A.G. Medina, Infinite dilution activity coefficients predicted by UNIFAC group contribution, Ind. Eng. Chem. Res. 27 (1988) 1269–1277.
- [37] H.K. Hansen, P. Rasmussen, A. Fredenslund, M. Schiller, J. Gmehling, Vapor-liquid equilibria by UNIFAC group contribution. 5. Revision and extension, Ind. Eng. Chem. Res. 30 (1991) 2355–2358.
- [38] M. Romay, N. Diban, A. Urtiaga, Thermodynamic modeling and validation of the temperature influence in ternary phase polymer systems, Polymers 13 (2021) 678.
- [39] E. Favre, Q.T. Nguyen, R. Clement, J. Neel, Application of Flory-Huggins theory to ternary polymer-solvents equilibria: a case study, Eur. Polym. J. 32 (1996) 303–309
- [40] M. De bruyn, V.L. Budarin, A. Misefari, S. Shimizu, H. Fish, M. Cockett, A.J. Hunt, H. Hofstetter, B.M. Weckhuysen, J.H. Clark, D.J. Macquarrie, Geminal diol of dihydrolevoglucosenone as a switchable hydrotrope: a continuum of green manostructured solvents, ACS Sustain. Chem. Eng. 7 (2019) 7878–7883.
- [41] P.R. Bevington, D.K. Robinson, Data Reduction and Error Analysis for the Physical Sciences, third ed., McGraw-Hill, Massachusetts, 2003.
- [42] Y. Huang, D.R. Paul, Physical aging of thin glassy polymer films monitored by gas permeability, Polymer 45 (2004) 8377–8393.
- [43] D.F. Sanders, Z.P. Smith, R. Guo, L.M. Robeson, J.E. McGrath, D.R. Paul, B. D. Freeman, Energy-efficient polymeric gas separation membranes for a sustainable future: a review, Polymer 54 (2013) 4729–4761.
- [44] D. Wang, K. Li, W.K. Teo, Effects of temperature and pressure on gas permselection properties in asymmetric membranes, J. Membr. Sci. 105 (1995) 89–101.